JYX
JYVÄSKYLÄN YLIOPISTO
UNIVERSITY OF JYVÄSKYLÄ

This is a self-archived version of an original article. This version may differ from the original in pagination and typographic details.

Author(s): Hegazy, Sherif; Ibrahim, Hanan H.; Weckman, Timo; Hu, Tao; Tuomikoski, Sari; Lassi, Ulla; Honkala, Karoliina; Srivastava, Varsha

Title: Synergistic pyrolysis of Cellulose/Fe-MOF Composite : A Combined experimental and DFT study on dye removal

Year: 2025

Version: Published version

Copyright: © 2024 The Author(s). Published by Elsevier B.V.

Rights: CC BY 4.0

Rights url: https://creativecommons.org/licenses/by/4.0/

Please cite the original version:

Hegazy, S., Ibrahim, H. H., Weckman, T., Hu, T., Tuomikoski, S., Lassi, U., Honkala, K., & Srivastava, V. (2025). Synergistic pyrolysis of Cellulose/Fe-MOF Composite : A Combined experimental and DFT study on dye removal. Chemical Engineering Journal, 504, Article 158654. https://doi.org/10.1016/j.cej.2024.158654

Chemical Engineering Journal 504 (2025) 158654

Contents lists available at ScienceDirect

Chemical Engineering Journal

journal homepage: www.elsevier.com/locate/cej

Synergistic pyrolysis of Cellulose/Fe-MOF Composite: A Combined experimental and DFT study on dye removal

Sherif Hegazy [a], Hanan H. Ibrahim [b], Timo Weckman [b], Tao Hu [a], Sari Tuomikoski [a], Ulla Lassi [a], Karoliina Honkala [b,*], Varsha Srivastava [a,*]

[a] Research Unit of Sustainable Chemistry, University of Oulu, P.O. Box 4300, FI-90014 Oulu, Finland
[b] Department of Chemistry, Nanoscience Center, University of Jyväskylä, P.O. Box 35, FI-50015 Jyväskylä, Finland

ARTICLE INFO

Keywords:
Adsorption
Biochar
Cationic dye
Density functional theory
Pyrolysis
Metal organic framework
Water treatment

ABSTRACT

We propose the development of an innovative composite material formed through the pyrolysis of oxidized cellulose derived from sawdust, utilizing iron-based MOF as a precursor. This novel material incorporates multiple iron-based components (Fe_3O_4, Fe_3C and Fe^0) within a biochar matrix. We employed the composite to adsorb a cationic dye from aqueous solution. Batch adsorption studies explored the effects of pH, contact time, and initial dye concentration. The experimental data fitted well with the pseudo-second-order kinetic model, suggesting chemisorption as the primary mechanism, while equilibrium adsorption results fitted to the Langmuir isotherm model, described monolayer adsorption displaying the highest adsorption capacity (106 mg/g). A fixed-bed column experiment further demonstrated effective removal of methylene blue (MB) dye, achieving an initial breakthrough time of approximately 12 h, and exhibiting an adsorption capacity (q_e = 71.14 mg/g) surpassing batch adsorption capacity at the same concentration (q_e batch = 52.53 mg/g), signifying the practical utility of the materials. In addition, pyrolysis-derived biochar samples displayed improved total organic carbon (TOC) removal efficiency, with P-Cell-MOF achieving 93 % TOC removal. Density functional theory (DFT) calculations were employed to investigate the binding of MB on the various materials derived from the pyrolysis of cellulose with MOF. The calculations show that MB chemisorbs on both Fe(110) and Fe_3C(001) surfaces while only physisorption was observed on Fe_3O_4(111) and graphene. These computational findings align well with the experimental data and provide an explanation for the enhanced TOC removal observed with the P-Cell-MOF.

1. Introduction

Waterborne diseases are a pervasive global challenge, impacting more than 2.3 billion individuals, particularly in developing nations [1,2]. Water sources can contain various harmful substances such as heavy metals, polyaromatic hydrocarbons, and dyes. When the levels of these contaminants exceed safe limits, the water becomes unsuitable for human consumption [3]. Notably, the textile dyeing industry discharges wastewater loaded with synthetic dyes, further worsening this issue. Among these dyes, methylene blue (MB) is prevalent, utilized in applications like dyeing, chemical indicators, and biomedicine. However, MB's extensive use raises concerns due to its potential health and environmental risks, including conditions like meningitis, neuronal cell apoptosis, and symptoms like nausea and vomiting [4].

A variety of methods have been used to address wastewater pollution, such as membrane filtration [5], flocculation [6], co-precipitation [7], photodegradation [8], biological treatment [9]. Among these, adsorption onto porous materials has proven to be the most effective because of its low cost and high efficiency, operational simplicity, and environmentally friendly nature [10]. Governments increasingly acknowledge the importance of developing sustainable carbon materials to address both environmental issues and economic stability. Carbon materials are highly versatile, finding applications in various fields such as energy and environmental sciences [11]. Graphitic carbon is favored for its exceptional chemical stability, large surface area, and excellent thermal and electrical conductivity [12]. Bio-derived materials are especially promising for the sustainable production of graphitic carbons [3]. Biochar has been widely utilized in various fields, most notably as an adsorbent for removing pollutants from water, including heavy metals and dyes [13]. Pristine biochar surfaces generally carry a negative charge because of the dissociation of oxygen-containing functional groups [14]. To enhance their adsorption capacity for specific

* Corresponding authors.
E-mail addresses: karoliina.honkala@jyu.fi (K. Honkala), varsha.srivastava@oulu.fi (V. Srivastava).

https://doi.org/10.1016/j.cej.2024.158654
Received 18 September 2024; Received in revised form 12 December 2024; Accepted 14 December 2024
Available online 19 December 2024
1385-8947/© 2024 The Author(s). Published by Elsevier B.V. This is an open access article under the CC BY license (http://creativecommons.org/licenses/by/4.0/).

contaminants, biochar properties have been systematically modified through various physical and chemical methods. Within literature, chemical activation has proven to be more effective than physical activation [15]. During physical activation, the raw material is subjected to carbonization at elevated temperatures in an inert atmosphere, typically using carbon dioxide (CO_2) or water vapor [16]. In contrast, chemical modification entails carbonization through a reaction with specific chemicals in an inert environment at elevated temperatures. These chemical agents, as reported in previous studies, have demonstrated their efficacy in enhancing biochar's adsorption capacity for a range of target contaminants [17,18].

Iron, being one of the most plentiful metals in the Earth's crust, is frequently used in modifying biochar to produce iron-biochar composites. Research indicates that the presence of zero valent iron (Fe^0) in these composites enhances both reduction and surface adsorption processes, making them effective for removing both methylene blue and acid orange 7 dye [19]. Among the notable members of the iron-based materials family, iron carbide Fe_3C is notable for its unique properties, including high crystallinity and outstanding stability. Existing literature provides evidence that Fe_3C demonstrates exceptional efficiency in removing methyl orange over a wide pH range [20]. The combination of zero valent iron (Fe^0) with iron carbide (Fe_3C) further enhances their reactivity and stability while reducing their toxicity [21]. In recent years, metal–organic frameworks (MOFs) have gained huge attention in various application including water treatment. Iron based metal–organic frameworks (MOFs) including MIL-100(Fe), Fe-BTC MOF, MIL-88(Fe), MIL-53(Fe) etc. have been utilized in wastewater treatment. Additionally, the use of MOFs to produce carbon-embedded metal nanoparticles is a highly adaptable technique. A key advantage of this approach is the wide variety of MOF structures available, allowing for flexibility in selecting the optimal active metal [22]. These composites, referred to as M@C, where 'M' signifies the metal or metal oxide nanoparticle, have been extensively studied in numerous syntheses, with examples such as Co@C, Fe@C, and Fe_2O_3@C. These materials have found utility across a spectrum of applications, ranging from batteries and magnetic materials to processes involving aqueous solution separation and their role as catalysts for oxygen reduction in fuel cells [23–25].

In this study, our objective is to create an innovative composite material that incorporates multiple phases of iron compounds within a biochar matrix. Both native cellulose and cellulose-MOF based composite (both before and after the pyrolysis process) will be compared for the elimination of cationic dyes from water solutions. Density functional theory (DFT) calculations are employed to assess the MB binding properties on materials providing insights into how pyrolysis enhances MB removal. As far as we are aware, this is the first instance of utilizing this unique composite structure for dye removal.

2. Experimental

2.1. Materials

Spruce sawdust served as the main raw material, was obtained from a sawmill in Northern Sweden. Polyvinyl Alcohol (PVA 7200, with a degree of hydrolysis of 86 %) was sourced from RanReac AppliChem (Spain). Hydrochloric Acid (HCl), Sodium Hydroxide (NaOH), and Sodium Hypochlorite (NaClO, 15 % active Cl_2) were purchased from VWR (France). Iron (III) Chloride ($FeCl_3$, >98 % purity) was acquired from Merck (Germany). Trimesic Acid (H_3BTC, 95 % purity) was sourced from Sigma Aldrich (Germany). 2,2,6,6-tetramethylpiperidinyl-1-oxyl (TEMPO) was obtained from Apollo Scientific (United Kingdom). Sodium Bromide (NaBr, 99 % purity) was purchased from J.T.Baker (Netherlands). Methylene Blue (MB) dyes were obtained from Thermo Fisher Scientific (UK).

2.2. Experimental methods

2.2.1. Synthesis of Fe-BTC MOF

In this study, iron based MOF, Fe-BTC MOF was synthesized following the procedure outlined in [26]. In brief, 5.08 g of $FeCl_3$ was dissolved in 100 mL of DI water. A solution containing 2.63 g of Trimesic acid, 36.85 mL of 1.06 M NaOH, and 63.88 mL of H_2O was gradually added to the $FeCl_3$ solution with continuous stirring. The resulting solid was collected by centrifugation, rinsed with DI water, and left to air-dry.

2.2.2. Synthesis of TEMPO-Oxidized cellulose Nanofibers

Cellulose fibers were initially extracted from spruce sawdust following a previously published method [27]. In this process, 50 g of cellulose fibers were suspended in 3 L of water containing 0.625 g of TEMPO and 6.25 g of sodium bromide. A solution of NaClO (11.63 mL, 12 %) was added to the mixture. The pH was carefully maintained at 10 by gradually adding 0.5 M NaOH, monitored with a pH meter until the pH stabilized. The resulting TEMPO-oxidized cellulose was thoroughly rinsed with water using a filter sieve until a neutral pH was achieved. The oxidized cellulose was then frozen and freeze-dried at −60 °C and 0.1 mbar.

2.2.3. Synthesis of composite aerogel and Carbon-MOF aerogel

To prepare the (O-cellulose) aerogel, 4 g of oxidized cellulose was mixed with 100 mL of a 4 % PVA solution and fibrillated using a high-pressure homogenizer (APV-2000, 100 MPa) for 15 min. Subsequently, 6 mL of a 5 % PVA solution was added, and the mixture was left in an oven for overnight at 75 °C for complete crosslinking. The same procedure was repeated to prepare (O-Cellulose-MOF) aerogel by adding Fe-BTC MOF (0.2 g, 5 % of cellulose mass) before the crosslinking step. Both types of aerogels were then subjected to pyrolysis under a nitrogen flow (2 L/min). The TEMPO-oxidized cellulose nanofiber (TOCN) aerogels were initially heated to 500 °C at a rate of 2 °C/min, held at this temperature for 1 h, and then raised to 600 °C at the same rate for another hour. Afterward, the temperature was increased to 900 °C at a rate of 5 °C/min, where it was maintained for 2 h to complete the pyrolysis process. The samples were then allowed to cool naturally to room temperature, resulting in pyrolyzed cellulose named (P-Cellulose) and pyrolyzed cellulose named (P-Cell-MOF), as shown in Fig. 1.

2.3. Characterization

To investigate the properties, synthesized material was thoroughly characterized [13,19,28], and all characterization details are provided in of the Supplementary Information (**Section S1**).

2.4. Adsorption studies

The removal of (MB) dye through adsorption was examined using both batch and column techniques. The experimental procedures are outlined below.

2.4.1. Batch experiments

For batch experiments, MB dye concentrations were quantified spectrophotometrically at the wavelength of maximum absorbance ($\lambda_{max} = 663$ nm) [29]. For each experiment, 0.02 g of the adsorbent was added to 10 mL of MB solutions at a concentration of 60 mg/L, with pH values of 3, 5, 7, and 9. Several parameters were analyzed, such as contact time (1, 2, 3, 4, 5, 6, 12, and 24 h), initial dye concentrations (25 mg/L, 50 mg/L, 100 mg/L, 200 mg/L, 300 mg/L, 400 mg/L, and 500 mg/L), and temperature (5 °C, 22 °C, 35 °C, and 45 °C). Adsorption kinetics and isotherms were investigated in these batch experiments. The dye removal efficiency (%E) and adsorption capacity (q_e, mg/g) were calculated using the following formulas:

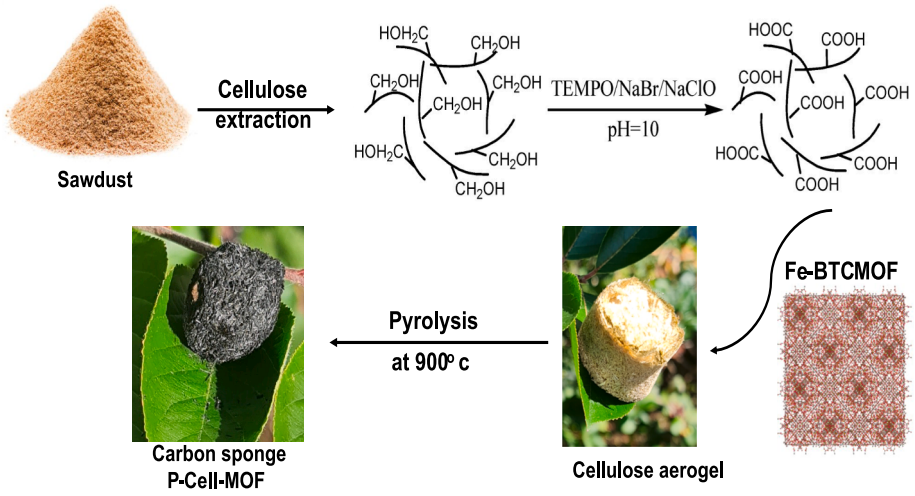

Fig. 1. Schematic representation of the procedure for synthesizing P-Cell-MOF sample.

$$\%E = \frac{C_0 - C_e}{C_0} \times 100 \quad (1)$$

$$q_e = (C_0 - C_e)\frac{V}{m} \quad (2)$$

Where C_o and C_e (mg/L) represent the initial and final concentrations of MB, respectively. V(L) is the volume of the MB solution in liters, and m is the mass of the adsorbent in grams.

2.4.1.1. Column experiments. For the column adsorption studies, a fixed bed of P-Cell-MOF (1.5 g) adsorbent was created by casting it in a plastic column measuring 6 cm in height and 2 cm in internal diameter. To prevent adsorbent loss, mesh sieves with a 0.45 μm PTFE (polytetrafluoroethylene) membrane filter were placed at both the inlet and outlet. The total column volume was 0.0188 L. Dye solution was introduced into the column from the bottom using a peristaltic pump, and effluent samples were collected from the top at regular intervals for analysis. The solution flow rate was consistently maintained at 2 mL/min throughout the experiment, in line with previous research conducted by our group [30]. The experiment was carried out at a constant temperature of 20 °C, with an initial dye concentration of 100 mg/L and neutral pH, based on parameters from the batch experiments. The column's dynamic behavior was evaluated using a breakthrough curve, which plots the ratio of effluent dye concentration at time "t" to the initial dye concentration (C_t/C_0) against time. The adsorption capacity of the column (q_e, mg/g) measures the amount of MB dye adsorbed per gram of adsorbent until saturation. In this study, the saturation point is defined when C_t/C_0 reaches 0.6. The adsorption capacity is determined by the following equation:

$$q_e = \frac{C_0 Q}{1000 m_{ads}} \int_0^{ts} \left(1 - \frac{C(t)}{C_0}\right) dt \quad (3)$$

Where C_0 represents the MB dye concentration in the feed (mg/L), Q is the volumetric flow rate (mL/min), and m_{ads} is the mass of the adsorbent (g) [31].

2.5. Desorption and regeneration experiments

To evaluate the reusability of the P-Cell-MOF adsorbent, a set of desorption and regeneration tests was performed. After the adsorption of MB dye from the aqueous solution, P-Cell-MOF adsorbent was subjected to a cleaning process using 70 % ethanol, accompanied by rinsing with deionized water. The regenerated adsorbent was then reused for the removal of MB dye from the aqueous solution. After each regeneration cycle, the MB dye concentration in the filtrate was analyzed using UV–visible spectroscopy. The recyclability of the mixed metal P-Cell-MOF was assessed by conducting five cycles for MB adsorption.

2.6. Density functional theory calculations

2.6.1. Computational details

The electronic structure calculations were carried out using spin-polarized density functional theory (DFT), as implemented in the GPAW software [32,33]. The grid-based finite difference method was used for solving the Kohn-Sham equations with grid spacing of 0.24 Å for Fe_3O_4, 0.20 Å for Fe_3C and 0.18 Å for graphite and Fe metal surface. The exchange–correlation functional proposed by Perdew, Burke and Ernzerhof (PBE) [34] was used, along with the D4 dispersion correction by Grimme [35] For Fe_3O_4, the DFT + U was applied to the *d*-electrons of Fe, using a 4.9 eV correction determined from a linear-response calculation on the primitive bulk [36–38].To account for the solvent/solute interactions, we used the Continuum Solvent Model (CSM) [39] to calculate the adsorption of a neutral MB molecule on all investigated surfaces. For calculations involving a charged MB cation, we employed the Solvated Jellium Method (SJM) [39,40]. All geometry optimization calculations were performed until the atomic forces were below 0.05 eV/Å.

The adsorption energies for a MB chloride (MB-Cl) molecule, were calculated as

$$E_{ads} = E_{tot} - E_{surf}^{CSM} - E_{ads}^{CSM} \quad (4)$$

where E_{tot} the total energy of the surface and the adsorbed molecule, E_{surf}^{CSM} is the energy of the bare surface and E_{ads}^{CSM} is the energy of the adsorbed molecule. The reference surface and MB energies were calculated using the continuum solvent model (CSM).

2.6.2. Surface models

The graphite surface was mimicked by a single graphene layer with a $p(8 \times 5)$ unit cell together with a $(1 \times 2 \times 1)$ k-point sampling. For bulk bcc-Fe, the calculated lattice constant and magnetic moment are 2.91 Å and 2.19 μ_B respectively, in line with experimental values of 2.86 Å and 2.22 μ_B [41,42]. A $(6 \times 5 \times 3)$ slab was used to represent the most stable Fe(110) surface, with the bottom layer fixed into its bulk positions and a $(2 \times 2 \times 1)$ k-point mesh was employed to sample the reciprocal space.

Crystalline θ-Fe_3C has an orthorhombic lattice in the space group *Pnma*. Our calculated lattice parameters, $a = 4.491$ Å, $b = 5.030$ Å, and $c = 6.739$ Å, and magnetic moments (Fe_g: 1.93 μ_B and Fe_s: 2.01 μ_B) agree

reasonably well with the experimental values ($a = 4.524$ Å, $b = 5.088$ Å, $c = 6.741$ Å and average magnetic moment of Fe, 1.78 μ_B) [43,44]. We chose the most stable θ-Fe_3C(001) to represent the surface of the iron-carbide having both exposed carbon and iron atoms [45]. The (001) surface was modelled as a 3 × 2 unit cells wide slab of 16 atomic layers thick, with the bottom 7 atomic layers fixed to their bulk positions. The reciprocal space was sampled using a 1 × 2 × 1 k-point mesh.

Ferrimagnetic Fe_3O_4 (magnetite) has a cubic inverse spinel crystal structure where iron exhibits both Fe^{2+} and Fe^{3+} oxidation states in the lattice with a tetrahedrally coordinated Fe^{3+} (Fe_A site) and an octahedrally coordinated Fe^{2+}/Fe^{3+} (Fe_B site) [46,47]. Local magnetic moments of Fe_A and Fe_B sites are oriented antiparallel to each other [48]. The computed lattice parameter of 8.56 Å is slightly larger than the experimental value; 8.378 Å [46]. For the bulk lattice optimization, a finer grid spacing of 0.2 Å was used. The calculated local magnetic moments of the iron atoms in bulk Fe_3O_4 were −4.13 and 4.13 μ_B for Fe_A and Fe_B sites, respectively, with total magnetic moment of 4.4 μ_B for Fe_3O_4 units. These values are slightly larger than previously reported experimental and computational ones [48,49]. While some studies have reported a small band gap of 0.2 eV for magnetite [48,50], our calculations indicate that bulk oxide is metallic. The (1 1 1) facet of Fe_3O_4 is the most stable among the six possible terminations [48,51]. We chose a Fe_{oct2}-termination, as it matches best with experimental data [52]. The hydroxylated Fe_3O_4(1 1 1) surface was adopted from ref. [52] as a model for MB adsorption. All the slab models include a 12 Å vacuum layer to prevent interactions between the repeated slabs.

3. Results and discussion

3.1. Characterization of adsorbent

The adsorbents' surface areas and structural properties were assessed using the Brunauer–Emmett–Teller (BET) method. The surface area, pore diameter, and pore volume data in Table 1 offer valuable insights into the textural attributes of these materials. Notably, O-cellulose and Cellulose-MOF demonstrated relatively modest surface areas, while P-Cellulose and P-Cell-MOF exhibited significantly higher surface areas (436 m^2/g), indicating the successful conversion of cellulose into high-surface-area materials through the pyrolysis process [53]. Moreover, the variance in pore diameter and pore volume profiles across the samples highlights distinct porosity characteristics, with P-Cellulose and P-cell-MOF displaying a notable dominance of micropores and the absence of macropores, further emphasizing the textural transformations achieved during pyrolysis. The nitrogen adsorption–desorption isotherms **(**Fig. 2**a and b)** observed before the pyrolysis process closely resembled type II isotherms according to the IUPAC classification. However, after pyrolysis **(**Fig. 2**c and d)**, the isotherms exhibited a shift towards a typical type-IV behavior noticeable Hysteresis loops, typically classified as Type H4 [54]. The rapid adsorption increases at low relative pressure, indicates micropore filling, a defining trait of microporous materials. This observation suggests a significant presence of micropores within the post-pyrolysis carbon fiber structure, which significantly enhances the material's adsorption capabilities [55,56].

O-Cellulose was synthesized by converting the hydroxyl groups of extracted cellulose into carboxylic groups using the TEMPO oxidant. The success of the TEMPO oxidation reaction was verified by recording DRIFT spectra for both TEMPO-cellulose and native cellulose **(**Fig. 3**a).** Notably, when compared to native cellulose, TEMPO-cellulose displayed a more prominent peak at 1608 cm^{-1}, which corresponds to the C=O stretching of carbonyl groups in the carboxylic acid functional groups [57]. The FTIR spectra of oxidized cellulose before and after pyrolysis (O-cellulose, P-cellulose), Fe-BTC-MOF, and cellulose-MOF, both before and after pyrolysis, were analyzed and are presented in (Fig. 3**b).** The principal characteristic absorption peaks observed in these spectra are detailed as follows: In the spectral region of 3600 − 3100 cm^{-1}, a broad band centered at ~3339 cm^{-1} represents the O-H stretching vibration of hydroxyl groups within cellulose and water molecules. Additionally, there is a bending vibration of –OH groups at 1638 cm^{-1}, and a stretching band of CH groups at 2930 cm^{-1}. Notable peaks are observed at 893 cm^{-1}, 1019 cm^{-1}, and 1156 cm^{-1}, corresponding to the C-H bond, C-O bending vibration, and C−O−C of the β-glycosidic linkages, respectively [58,59]. In the Fe-BTC MOF spectrum, the broad band between 3200 and 3600 cm^{-1} is due to the O-H stretching of adsorbed water. The bands at 1620 and 1568 cm^{-1}, as well as at 1445 and 1374 cm^{-1}, are attributed to the asymmetric and symmetric stretching of the carboxylate groups of Fe-BTC, respectively. Peaks between 760 and 650 cm^{-1} are linked to the bending of aromatic C-H bonds [60]. In the cellulose-MOF sample, peaks similar to those in O-cellulose were observed, along with absorption peaks at 1147 and 1303 cm^{-1}, which correspond to the symmetric and asymmetric –C–O–C– stretching bands of the ester group in H_3BTC, suggesting that ester bonds may form between the MOF and CMF [61]. It is noteworthy that after pyrolysis, hydrophilic functional group peaks such as C=O, C–O, and –OH are notably absent, indicating a shift towards hydrophobicity in the materials [62].

XRD analysis was employed to confirm both the synthesis of Fe-BTC and the transformation during pyrolysis. Initially, the XRD pattern of the Fe-BTC sample **(**Fig. 3**c)** revealed well-defined peaks at 2θ values of 19°, 24°, and 28°, consistent with literature reports for Fe-BTC-MOF [60,63] affirming the successful synthesis. Additionally, the values of 2θ at 26°, 43°, 44°, 50°, 74°, and 90° are related to carbon, suggesting that biomass has transformed into graphite (ICDD: 00–060-0053, 04–015-2407). Subsequently, the XRD pattern of the pyrolyzed cellulose MOF sample **(**Fig. 3**c)** demonstrated characteristic peaks at 2θ values between 39° to 43°, in line with the reference code for cementite (Fe_3C) (ICDD: 04–008-9572), confirming the transformation. Additionally, a set of peaks located at 2θ = 30°, 35°, 57°, and 63° can be assigned to magnetite (Fe_3O_4) (ICDD: 01–088-4625). The appearance of iron metal peaks at 2θ = 43.3°, 50.4°, and 74° (ICDD: 04–002-3692) further substantiated the structural changes occurring during pyrolysis. This sequential analysis establishes the synthesis of Fe-BTC as a precursor to its subsequent transformation into cementite (Fe_3C) and magnetite (Fe_3O_4) during the pyrolysis process. These structural changes were also corroborated by EFTEM analysis.

To investigate the potential active sites of P-Cell-MOF for MB adsorption, XPS spectra were determined before and after the adsorption **(Fig. S1).** As depicted in (Fig. 4**a and c)**, four peaks of C 1s were detected at binding energies of approximately 284.7 eV, 285.8 eV, 287.3 eV, and 288.8 eV, which were assigned to C–C, C–O, C=O, and O-C=O, respectively. The relative proportions of these peaks were

Table 1
Textural properties of O-cellulose, Cellulose-MOF, P-cellulose, and P-cellulose-MOF.

Adsorbents	Surface area (m^2/g)	Pore diameter (nm)	Pore Volume (cm^3/g)	Micropores %	Meso pores %	Macro pores %
O-cellulose	0.8	4.4	0.001	8.33	66.67	25
Cellulose-MOF	1.7	5.9	0.004	10.26	64.10	25.64
P-Cellulose	436	1.8	0.180	68.58	30.93	0.49
P-cellulose-MOF	436	2.2	0.230	87.57	12.32	0.11

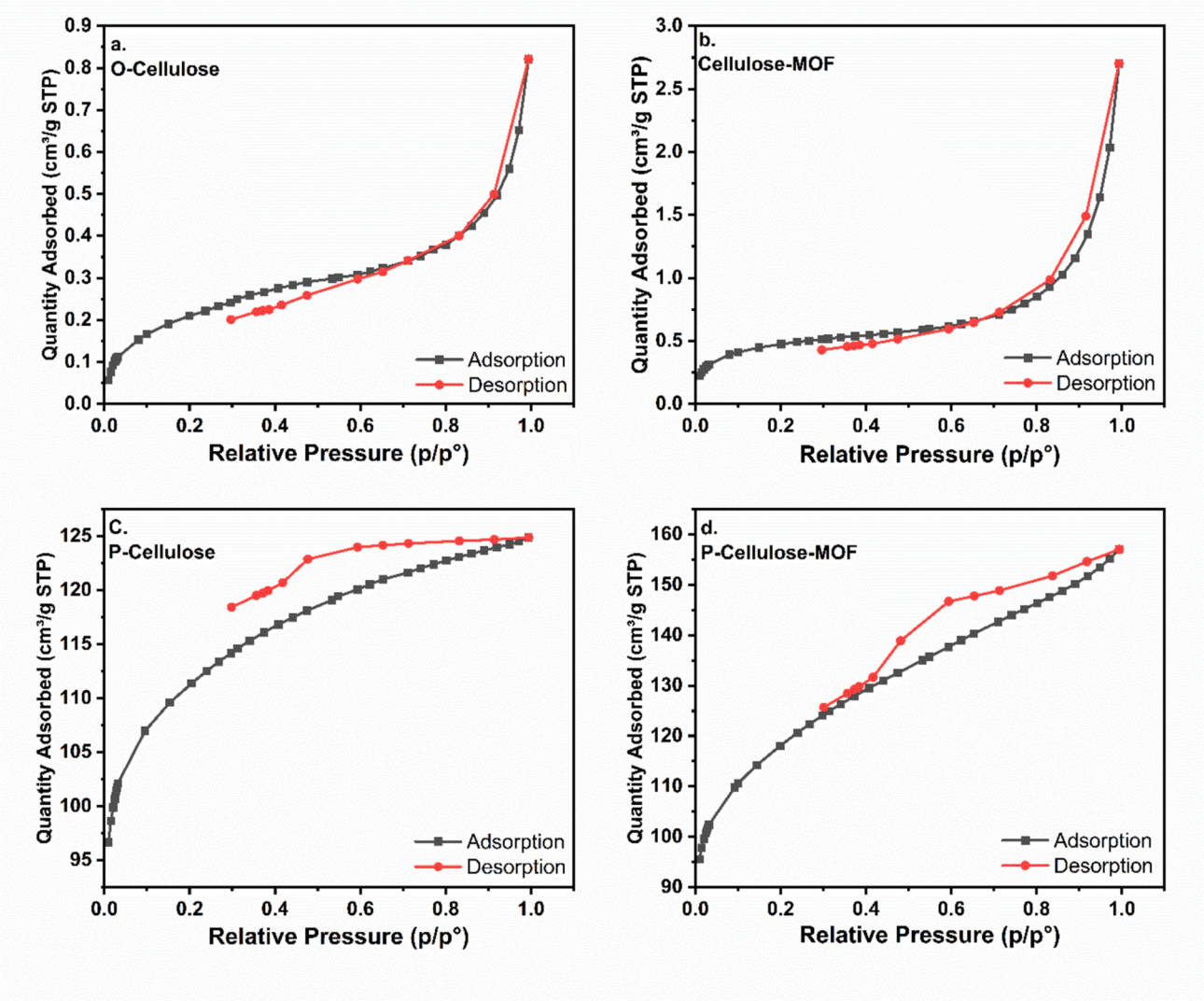

Fig. 2. N_2 adsorption–desorption isotherm plot of **a)** O-cellulose, **b)** Cellulose-MOF, **c)** P-cellulose, and **d)** P-cellulose-MOF.

calculated to be 57.33 %, 14.43 %, 5.69 %, and 2.69 %, respectively. Following the adsorption process, the relative contents of C–C, C–O, C=O, and O-C=O shifted to 32.19 %, 7.01 %, 2.79 %, and 1.63 %, respectively. Similarly, the O 1s spectrum **(**Fig. 4**b and d)** revealed the presence of four distinct peaks at around 530.5 eV, 532.1 eV, 533.5 eV, and 535.6 eV, corresponding to Fe–O, C–O, –COOH, and H_2O, respectively. After the adsorption, the relative ratios of Fe–O, C–O, –COOH, and H_2O increased from 3.81 %, 1.82 %, 1.39 %, and 1.23 % to 29.26 %, 15.15 %, 1.01 %, and 1.66 %, respectively. Notably, after adsorption, Fe 2p peaks appeared on the surface **(**Fig. 4**e),** with the maximum binding energy of the Fe $2p_{3/2}$ and Fe $2p_{1/2}$ observed at 724.7 eV and 711.1 eV, respectively, while the Fe–C peak was identified at 712.75 eV [64]. It can be inferred that Fe metal and Fe_3C are key players in the adsorption mechanism, enhancing the material's ability to capture and retain dye molecules.

In the FESEM analysis, the biochar material exhibited a prominently porous architecture, as illustrated in **(**Fig. 5**a** and Fig. 5**b).** Notably, the images also revealed the presence of well-defined crystalline ferric compounds embedded within the biochar matrix. This observation underscores the creation of a hierarchical porous carbon framework that hosts iron compounds, potentially serving as the active sites for the removal of MB dye. In the SEM-EDX analysis revealed the elemental composition of the P-Cell-MOF, with carbon being the predominant element at 85.2 %, followed by oxygen at 9.3 %, and iron at 5.5 % **(**Fig. 5**c).** The color-coded mapping in demonstrated the spatial association of carbon with iron, suggesting the presence of iron carbides **(**Fig. 5**d).** Furthermore, there is a possibility of the coexistence of iron oxides alongside the iron carbides, adding a layer of complexity to the material's composition.

EFTEM analysis, as depicted in **(**Fig. 5**e)** and **(**Fig. 5**f)** provide crucial insights into the structural characteristics of the P-Cell-MOF composite. The images reveal a highly amorphous carbon matrix with distinct graphitic layers. Additionally, the TEM images revealed the nanocrystalline and monodisperse nature of the iron (Fe) particles derived from Fe-MOF. They also demonstrated the presence of Fe_3C and Fe_3O_4 crystals within the material, ranging in size from 50 to 100 nm. This finding is consistent with previous reports of similar carbon encapsulation structures in composite iron materials prepared via the pyrolysis process [22,65].

3.2. Batch adsorption study for MB removal

3.2.1. Effect of pH and point of zero charge (PZC)

The pH of the dye solution significantly influences adsorption by altering the surface charge of the adsorbent. The relationship between pH and the adsorption capacity of the cationic dye, MB is shown in Fig.6. Notably, when the pH exceeded the point of zero charge (pH_{PZC}) at around 3.4, there was a marked increase in MB adsorption capacity.

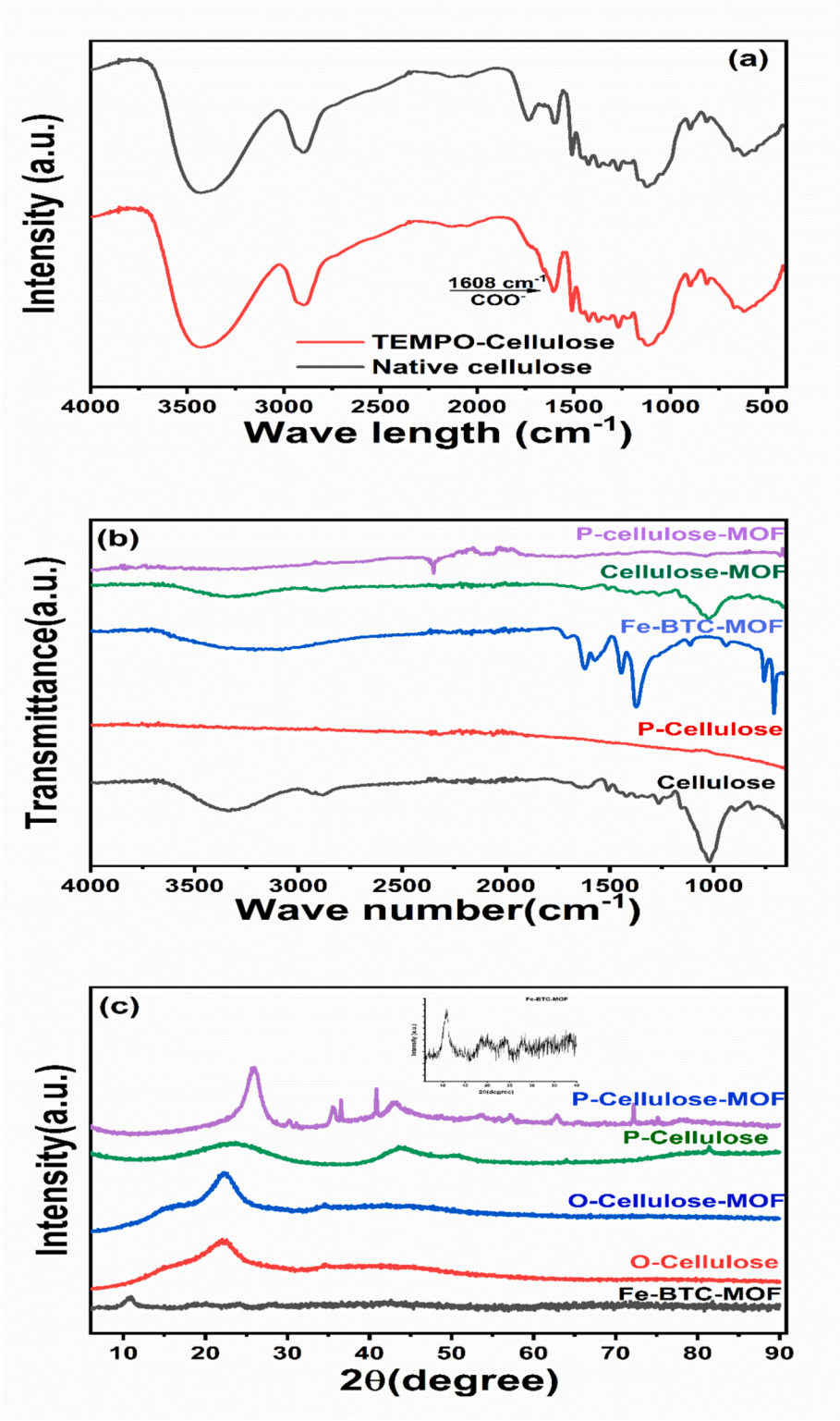

Fig. 3. **(a)** DRIFT spectra for TEMPO-Cellulose and native cellulose; **(b)** FTIR spectra and **(c)** XRD patterns Fe-BTC-MOF, O-cellulose, P-cellulose, and cellulose-MOF, P- cellulose-MOF.

Subsequently, this capacity became nearly constant within the pH range of 5.5 to 7. To explain this pH-dependent behavior, consider the surface charge of the adsorbent relative to the cationic MB adsorbate. When the initial pH is below the pH_{PZC}, the adsorbent's surface becomes positively charged due to proton (H^+) adsorption, hindering MB adsorption due to electrostatic repulsion. Conversely, when the solution pH exceeds the pH_{PZC}, the negatively charged adsorbent surface attracts cationic MB molecules, enhancing their uptake [66]. To investigate the iron leaching, adsorbent was tested under three different pH conditions (acidic, basic and neutral). Under acidic conditions, 0.002 mg/L iron concentration was measured in the solution which indicate minimal iron leaching and demonstrating the stability of the composite during the

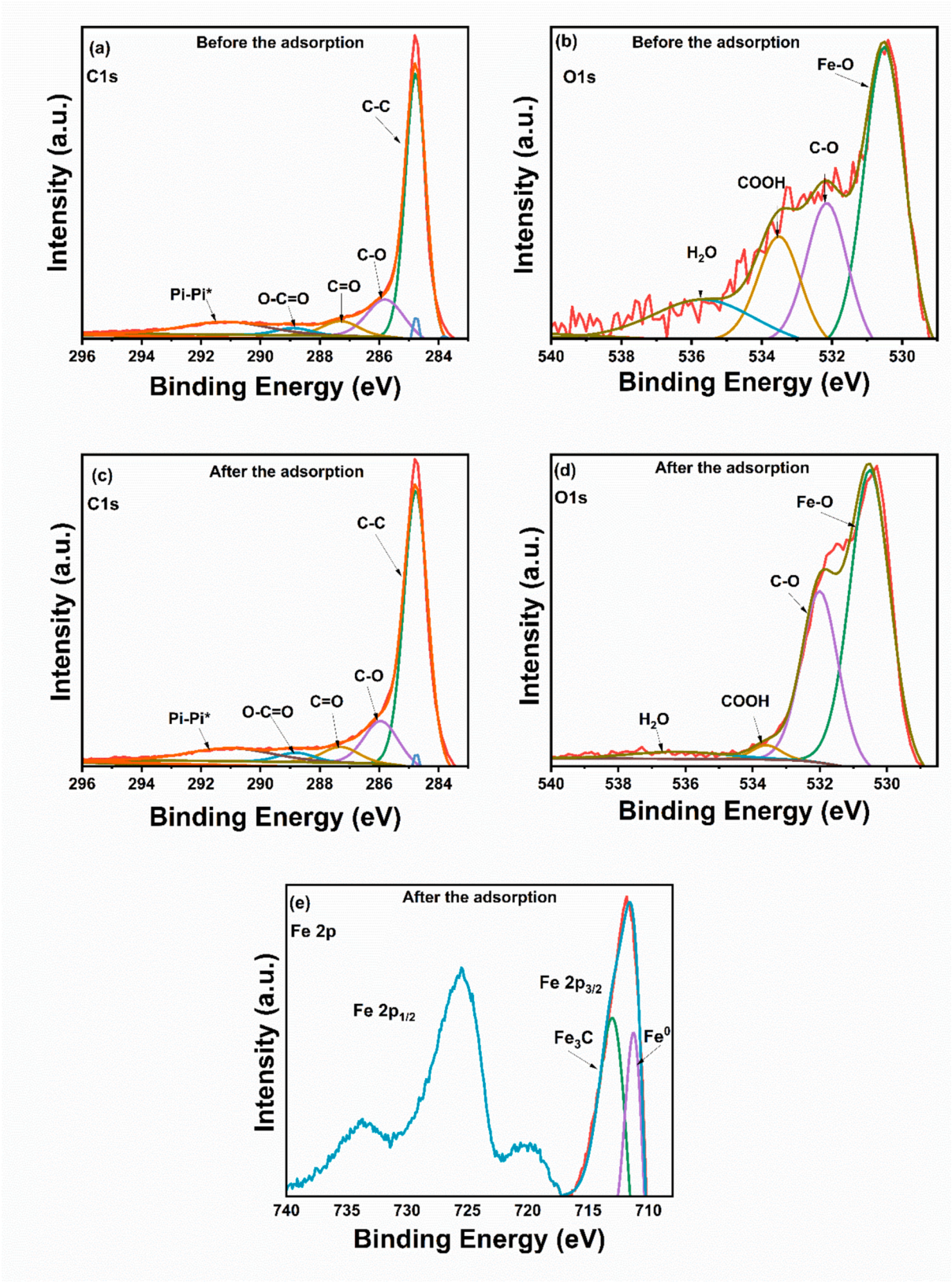

Fig. 4. High resolution XPS spectra of P-cellulose-MOF before and after MB adsorption.

adsorption process.

3.2.2. Effect of contact time and initial dye concentration

The dye solution concentration was tracked at various time intervals (from 1 to 24 h) using UV–visible spectroscopy, and the corresponding data are shown in (Fig. 7**a**). It is evident that dye removal increases with prolonged contact time, likely due to the abundance of vacant adsorption sites, allowing for rapid adsorption. The adsorption rate reaches

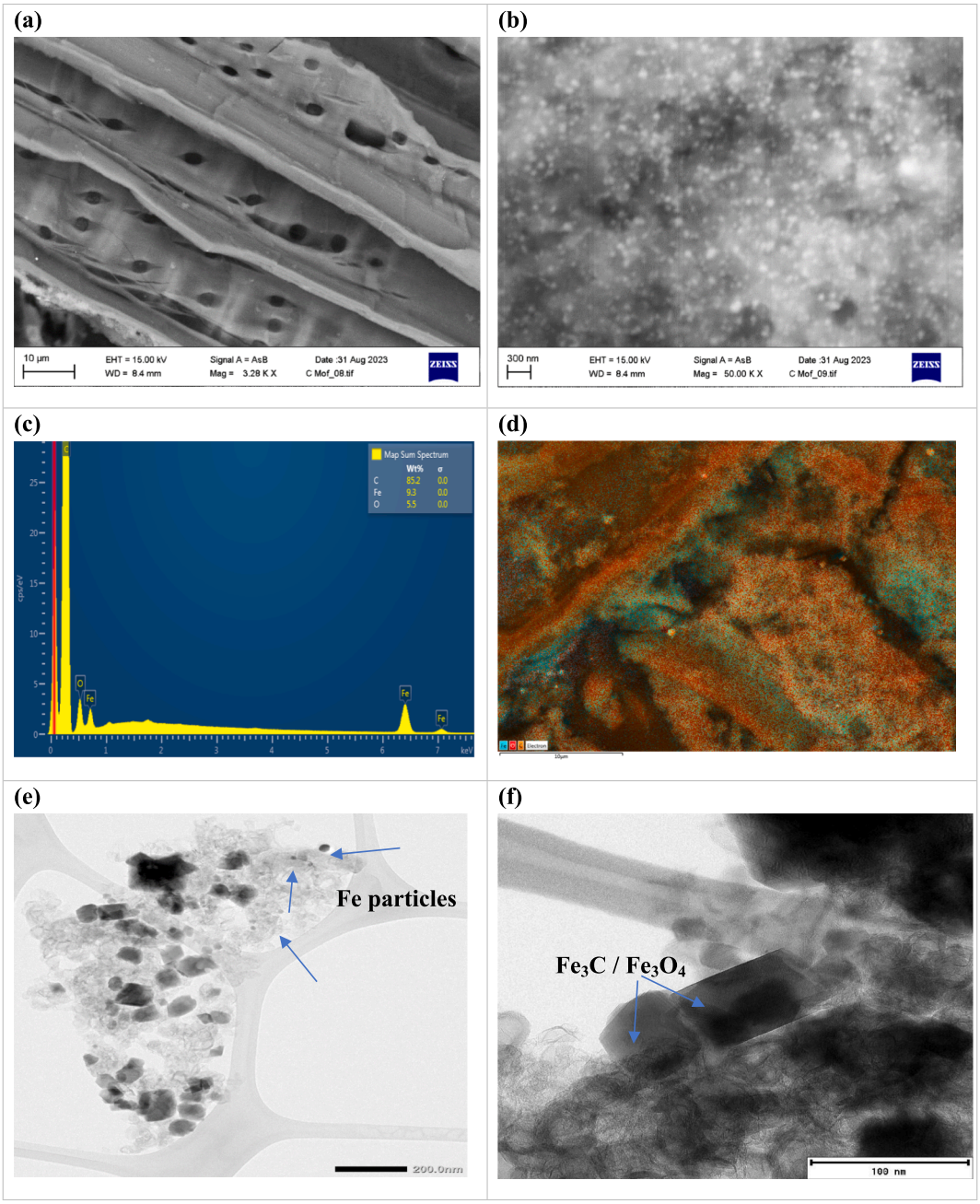

Fig. 5. **(a,b)** FESEM images of P- cellulose-MOF; **(c)** FESEM-EDS- elemental mapping; **(d)** Spectra of P- cellulose-MOF **(e,f)** EF-TEM images of P- cellulose-MOF.

equilibrium within approximately 6 h. Furthermore, the adsorption behaviour of MB dye was investigated over a concentration range of 25 mg/L to 500 mg/L at room temperature, and the results are presented in (Fig. 7**b**). It's noteworthy that the removal efficiency was notably higher at lower initial concentrations. This can be explained by the greater availability of vacant active sites at lower concentrations. However, when the initial concentration exceeded 250 mg/L, the removal efficiency declined. This reduction is likely due to the saturation of adsorption sites on the adsorbent surface, as higher concentrations result in fewer available active sites to accommodate all the MB molecules, leading to saturation [67]. It is important to highlight that the binding capacity for MB on P-cell-MOF was the highest among all samples, indicating the achievement of a high surface area (436 m^2/g). Additionally, the multiphase surface formed after pyrolysis, due to the coexistence of carbonized material and various iron phases, including Fe metals, Fe_3O_4, and Fe_3C aligns with the results of characterization, further enhancing the adsorption capacity [68]. However, the pyrolyzed cellulose exhibited the lowest adsorption capacity, due to the absence of all functional groups of oxidized cellulose after pyrolysis, as indicated by the FTIR and XRD results.

3.2.3. *Kinetics findings*

The adsorption kinetics of the dye onto P-Cell-MOF were evaluated using pseudo-first-order, pseudo-second-order, and Weber-Morris intraparticle diffusion (IPD) models **(Section S2).** The pseudo-second-order model demonstrated superior fit (average R^2>0.99), indicating chemisorption as the dominant adsorption mechanism. Calculated equilibrium adsorption capacities (q_e) closely matched experimental values, The Weber-Morris IPD model further detailed the adsorption mechanism, highlighting surface adsorption, inter-particle diffusion, and intra-particle diffusion as key factors. Detailed kinetics data are available in the supplementary materials **(Fig. S2, Table S1).**

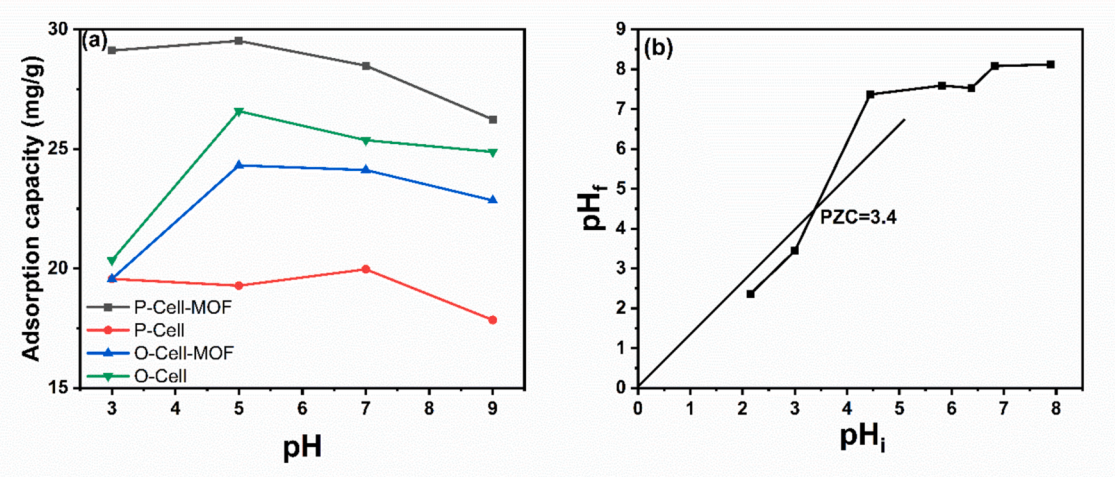

Fig. 6. **(a)** Effect of pH on the adsorption of MB dye (at 22 °C; time,6h; C_0 , 60 mg/L); **(b)** PZC of P-Cell-MOF.

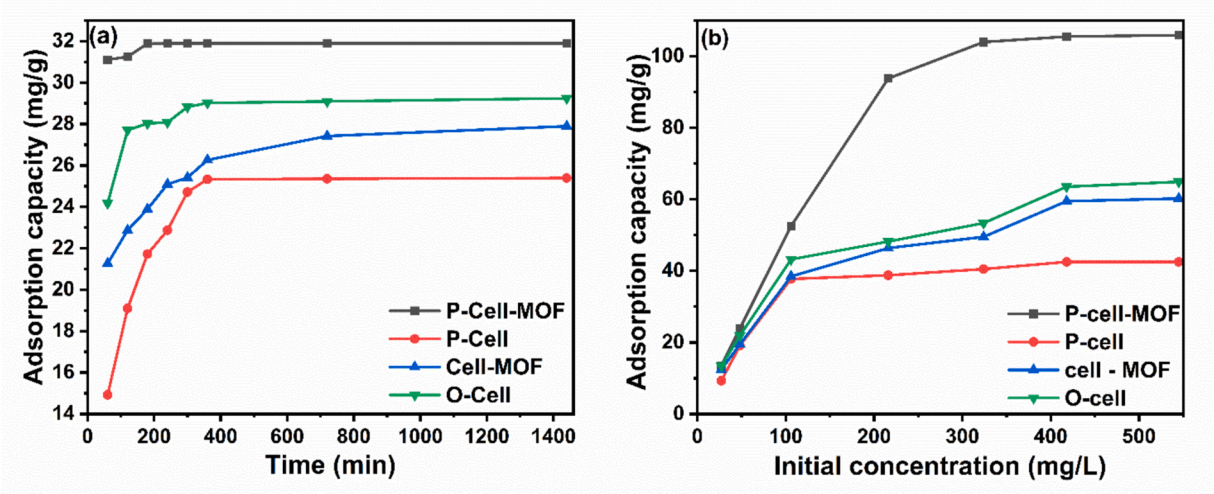

Fig. 7. **(a)** Effect of time on the adsorption of MB dye (at 25 °C; pH,5; C_0 , 60 mg/L); **(b)** Effect of initial concentration on the adsorption of MB dye (at 25 °C, time,6h; pH,5).

3.2.4. *Adsorption isotherms*

The adsorption isotherms of MB on P-Cell-MOF were characterized using Langmuir and Freundlich models **(Section S3)**. The Langmuir model, representing monolayer adsorption, exhibited excellent fitting ($R^2 > 0.99$), indicating homogeneous adsorption sites on P-Cell-MOF. The maximum adsorption capacity (q_m) was determined as 106 mg/g, surpassing the capacities of other reported adsorbents (Table 2) [4,69,70–75]. Complete isotherm plots and fitting parameters are available in supplementary **(Table S2 and Fig. S3).**

Table 2
Maximum adsorption capacity of MB by various adsorbents.

Adsorbent	Preparation method	q_m (mg/g)	Refs
Carbon nanotubes-graphene aerogels	Hydrothermal reduction	96.1	[69]
Wood waste-activated carbon	Carbonization	4.94	[70]
Biochar from liquefaction of rice husk	Thermochemical liquefaction	32.5–67.6	[71]
Carbon fiber aerogels	Air-limited calcination	102.2	[72]
Iron modified biochar	Pyrolysis	5.678	[73]
Cellulose aerogel	Freeze drying	29.7	[74]
Cellulose/PVA/Graphite foam	Freeze drying	110.81	[4]
P-Cell-MOF	Carbonization	106.38	This work

3.3. *Column adsorption study MB removal on P-Cell-MOF*

A column experiment using a fixed-bed setup was carried out to evaluate the effectiveness of the batch method in removing dye from industrial wastewater. In this experiment, a solution containing dye with an initial concentration of 100 mg/L was introduced into the fixed-bed column, flowing at a rate of 2 mL/min. After approximately 12 h, the concentration of the effluent reached nearly 60 % of the influent concentration (Supplementary video). An idealized breakthrough curve was generated by plotting the time of flow against C_t/C_o, as illustrated in **(**Fig.8**).** At $C_t/C_o \approx 0.60$, which signifies a 60 % breakthrough of the column, it was observed that this point was reached after approximately 700 min of MB dye adsorption. Importantly, the utilization of the fixed-bed column can be continued beyond the 60 % breakthrough until a 90 % breakthrough is achieved ($C_t/C_o = 0.9$) [75]. The calculated breakthrough parameters revealed that the adsorption capacity of the column ($q_e = 71.14$ mg/g) exceeded the batch adsorption capacity at the same initial concentration. This observation highlights the effectiveness of the fixed-bed column in dye removal and suggests its potential utility in

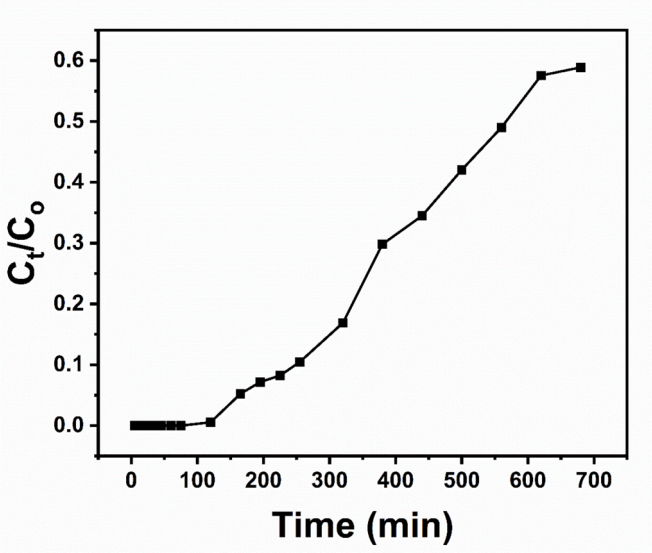

Fig. 8. Breakthrough curve for MB adsorption onto P-Cell-MOF in a fixed-bed process. Time contact was 700 min (11.6 h), Adsorbent mass was 1.5 g, an initial MB concentration (C_0) was 100 mg/L, at room temperature, neutral pH, and a flow rate of 1 mL/min.

treating industrial wastewater contaminated with this dye.

3.4. Total organic carbon (TOC) removal efficiency

The study investigated the Total Organic Carbon (TOC) removal efficiency of synthesized adsorbents, which is crucial for evaluating water quality by measuring organic carbon compounds in water. Remarkably, the pyrolysis-derived biochar samples outperformed their non-pyrolyzed counterparts. As demonstrated in (Fig. 9**a**), P-Cell-MOF achieved the highest TOC removal at 93 %, suggesting the potential for coupled adsorption-catalytic degradation mechanisms due to the presence of zero-valent iron produced after pyrolysis. P-Cell achieved 76 % TOC removal, while Cellulose showed 65 % efficiency, and Cell-MOF had slightly lower efficiency at 53.4 %.

3.5. Desorption of MB and reusability studies

The potential for reusing adsorbent materials in wastewater treatment is significant, both economically and environmentally. To evaluate the reusability of the P-Cell-MOF adsorbent, desorption and regeneration experiments were conducted through batch experiments. As depicted in (Fig.9**b**), the regenerated P-Cell-MOF exhibited remarkable reusability, maintaining its high adsorption capacity across multiple cycles. Specifically, over the course of five consecutive cycles, the adsorption percentages remained consistently high: 99.9 %, 90.2 %, 82 %, 78.7 %, and 74.9 %, respectively. These findings underscore the robustness and effectiveness of the adsorbent over repeated usage.

3.6. Computational analysis of MB dye on P-Cell-MOF adsorbent components

3.6.1. Water adsorption

Since the MB adsorption takes place in aqueous solution, a crucial question is whether there is adsorbed water on the substrate surface. To account for water content, we computed the adsorption energies for water on the studied surfaces. On $Fe_3C(001)$ and Fe(110) surfaces, multiple adsorption sites were considered for a single water molecule, while on $Fe_3O_4(111)$, the optimal adsorption structures for a single water molecule and a water dimer were adopted from ref [52]. For $Fe_3O_4(111)$, we calculated the adsorption energies, summarized in

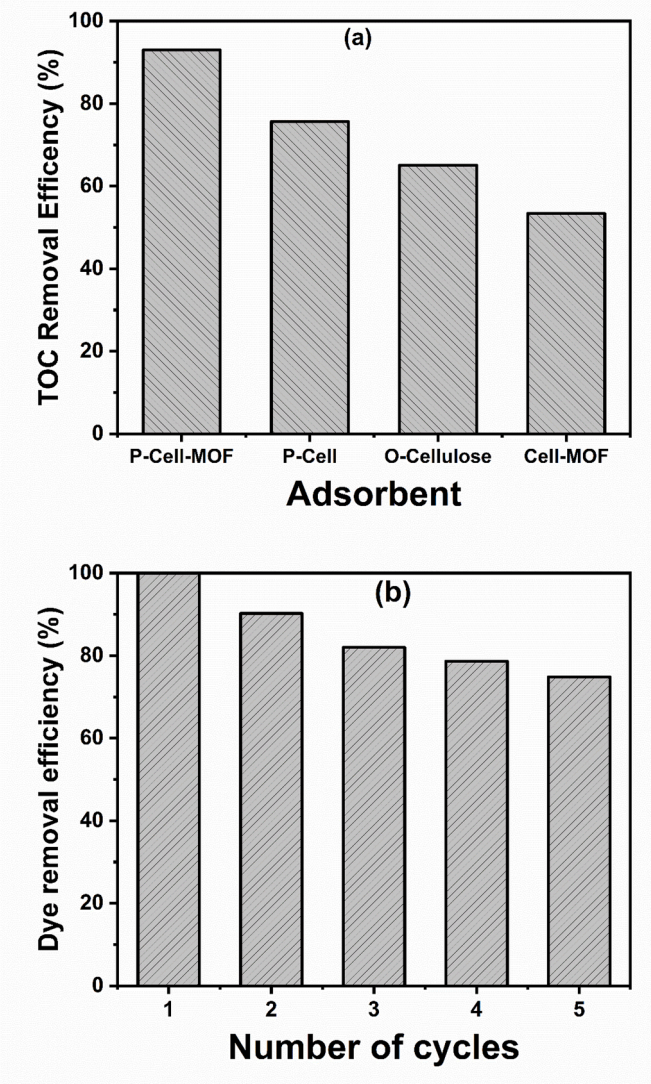

Fig. 9. (a) TOC removal efficiency for the different used adsorbents; **(b)** Recycle of removal efficiency of P-Cell-MOF for MB dye (at 25 °C; neural pH; C_0, 100 mg/L).

Table 3
Calculated water adsorption energies on the Fe(110), $Fe_3C(001)$, and $Fe_3O_4(111)$ surfaces. The adsorption energy in parenthesis for Fe_3O_4 corresponds to the average adsorption energy for the water dimer. All energies are in kJ/mol.

Surface	Adsorption energy
Fe(110)	−51
$Fe_3C(001)$	−57
$Fe_3O_4(111)$	−168 (−153)

(Table 3) both for a dissociative adsorption of a single water molecule and the average adsorption energy for a water dimer. In the case of the water dimer, the first water molecule dissociates on the oxide surface, while the second one binds intact close to the hydroxylated group (Fig. 10). We conclude that the adsorption of water on $Fe_3O_4(111)$ is very exothermic, while on $Fe_3C(001)$ and Fe(110) it is only moderately exothermic. The computed thermodynamics of water adsorption suggest that under reaction conditions, the $Fe_3O_4(111)$ surface becomes fully hydroxylated, whereas $Fe_3C(001)$ and Fe(110) surfaces remain bare, therefore the dimer structure on $Fe_3O_4(111)$ will be used as the model

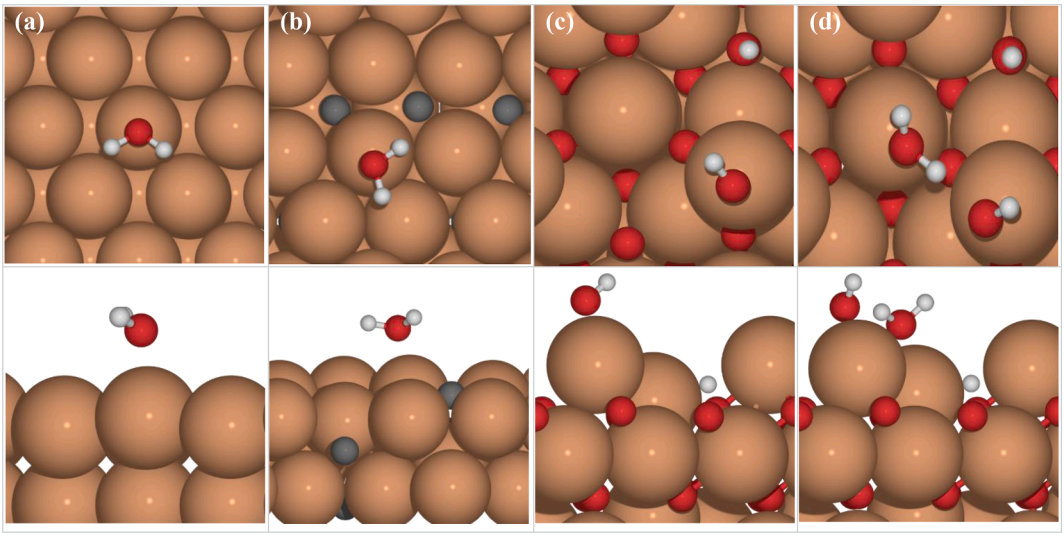

Fig. 10. The top- and side- views of the gas phase adsorbed water molecule on **(a)** Fe(110) and **(b)** $Fe_3C(001)$ surfaces, **(c)** and **(d)** the adsorbed water monomer and dimer on $Fe_3O_4(111)$ surface, respectively.

for the water covered surface. No other explicit solvent molecules will be included on the surface for simplicity.

3.6.2. *Adsorption of methylene blue dye*

To understand the high TOC removal observed in P-Cell-MOF, we used DFT calculations to investigate MB adsorption onto the components of P-Cell-MOF. Various adsorption geometries and sites were considered on different surfaces. Fig. 11 displays the most stable adsorption structures of MB chloride (MB-Cl) on each surface and Table 4 presents the corresponding adsorption energies. Our calculations show that the binding of a MB cation on Fe, Fe_3C and graphene surfaces and the MB binding trends (without the chloride anion) follow closely those of the neutral MB-Cl molecule, suggesting that a chloride anion plays no major role in adsorption thermodynamics. The adsorption structure and binding energies for MB cation are presented the supplementary materials **(Section S4, Fig. S4)**. On Fe(110) and Fe_3C (001) surfaces (see Fig. 11), MB-Cl interacts strongly with several surface Fe atoms, leading to a substantial distortion to the planar structure of the molecule. The strong interaction is reflected in highly exothermic adsorption energies, with the metallic Fe surface showing 150 kJ/mol more exothermic adsorption energies than the Fe_3C surface. On graphene, MB-Cl lies 3.34 Å above the surface and maintains its planar geometry, indicating that the molecule-surface interaction is physisorption, as supported by significantly less exothermic adsorption energy compared to the metallic and carbide Fe surfaces. On hydroxylated Fe_3O_4, MB remains in the planar configuration and is 2.75 Å above the surface. The lack of structural distortion suggests only a weak physisorption to the hydroxylated surface. The calculation of the adsorption energy was challenging due to varying magnetic moment distributions for the magnetite surface in the presence and absence of the adsorbate and no reliable value for adsorption energy was obtained for MB-Cl on Fe_3O_4. However, based on the optimized adsorption geometry, we can

Table 4
The calculated adsorption energies of MB Chloride adsorbed on Fe(110), $Fe_3C(001)$, $Fe_3O_4(111)$ and graphene. All the values are in kJ/mol.

Surface	Adsorption energy
Fe(110)	−648
$Fe_3C(001)$	−494
Graphene	−138

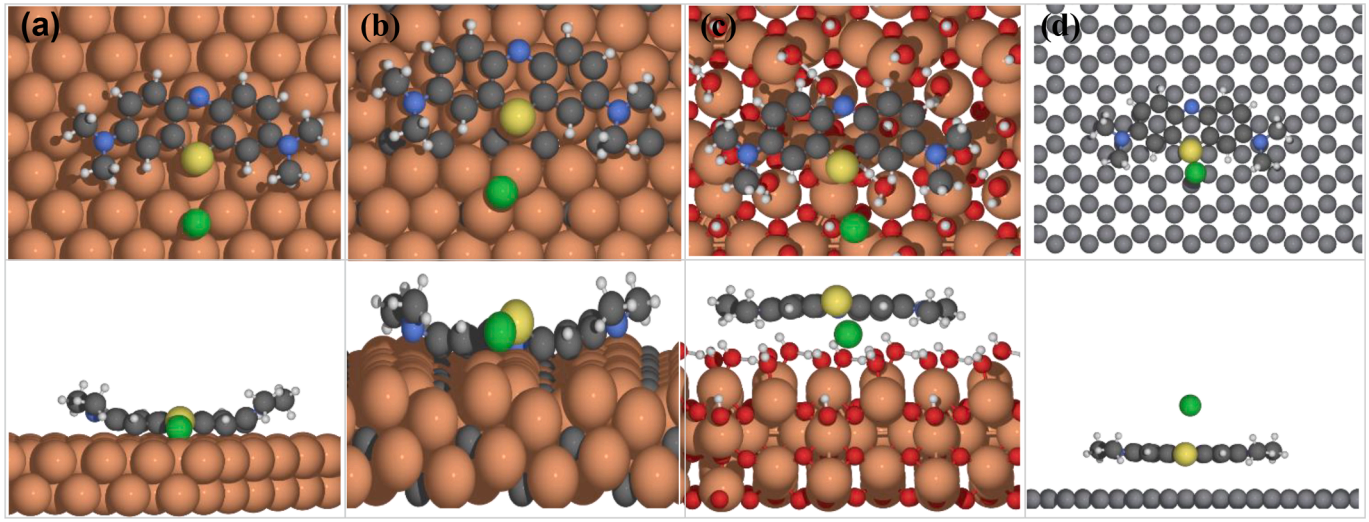

Fig. 11. Top and side views of methylene blue adsorption on **(a)** Fe(110), **(b)** $Fe_3C(001)$, **(c)** $Fe_3O_4(111)$ and **(d)** graphene surfaces.

conclude that due to hydroxylation, the adsorbate–surface interaction consists only of weak dipole–dipole and dispersion interactions between MB-Cl and the surface OH-groups. We estimate that MB-Cl adsorption energy is about the same order of magnitude or possibly slightly more exothermic than on graphene, but substantially weaker than on Fe and Fe_3C surfaces.

Our results suggest that MB-Cl chemisorbs on Fe and Fe_3C, while physisorption takes place on Fe_3O_4 and graphene. Thus, materials rich with surface Fe atoms bind MB, while this is not the case for carbon or hydroxylated surfaces. Difference in binding characteristics of MB provide an explanation for the improved adsorption capacity and TOC efficiency of P-Cell-MOF over the other materials considered in the present work experimentally: the pyrolysis of cellulose and MOF results in Fe and Fe_3C containing materials with Fe sites binding MB strongly, whereas these sites are missing from other adsorbents.

4. Conclusion

This study introduces an innovative composite material, P-Cell-MOF, developed through the pyrolysis of oxidized cellulose with Fe-BTC MOF. This synergistic process embeds multiple iron phases (Fe^0, Fe_3O_4, and Fe_3C) within a biochar matrix, significantly enhancing the material's adsorption properties. Characterization through XPS confirmed the pivotal role of Fe and Fe_3C in the adsorption mechanism, highlighting their contribution to the material's ability to capture and retain methylene blue (MB) dye. In batch adsorption studies, P-Cell-MOF demonstrated superior performance, achieving an impressive adsorption capacity of 106 mg/g for MB and a notable 93 % TOC removal efficiency. The pseudo-second-order kinetic and Langmuir isotherm models best described the adsorption process, indicating chemisorption and monolayer adsorption, respectively.

Both experimental results and computational DFT calculations supported the conclusion that P-Cell-MOF's enhanced performance is due to the strong chemisorption of MB on Fe and Fe_3C surfaces. DFT calculations showed that MB strongly interacts with Fe(110) and $Fe_3C(001)$ surfaces, leading to significant changes in the molecular structure and strongly exothermic adsorption. In contrast, physisorption was observed on graphene and hydroxylated Fe_3O_4 surfaces, with MB maintaining its planar geometry. This close agreement between experimental and computational results highlights the role of Fe metal and Fe_3C in providing active sites for effective MB adsorption. Fixed-bed column experiments underscored the practical utility of P-Cell-MOF, showcasing effective MB removal with an initial breakthrough time of approximately 12 h and a substantial adsorption capacity ($q_e = 71.14$ mg/g). Moreover, the material exhibited excellent reusability and robustness, reinforcing its potential for large-scale wastewater treatment applications.

CRediT authorship contribution statement

Sherif Hegazy: Writing – original draft, Methodology, Formal analysis, Data curation, Conceptualization. **Hanan H. Ibrahim:** Writing – original draft, Software, Data curation. **Timo Weckman:** Writing – review & editing, Supervision, Software. **Tao Hu:** Formal analysis, Data curation. **Sari Tuomikoski:** Writing – review & editing, Supervision. **Ulla Lassi:** Writing – review & editing, Validation, Supervision, Resources, Project administration, Funding acquisition. **Karoliina Honkala:** Writing – review & editing, Validation, Supervision, Resources. **Varsha Srivastava:** Writing – review & editing, Validation, Supervision.

Declaration of competing interest

The authors declare that they have no known competing financial interests or personal relationships that could have appeared to influence the work reported in this paper.

Acknowledgments

Sherif Hegazy acknowledges the financial support provided by the Finnish Cultural Foundation and the Black Green project (Project Number 2430480911). Hanan H. Ibrahim and Karoliina Honkala acknowledge funding from Business Finland (Project Synjet) and the Finnish Research Council (Project Number 351583). Hanan H. Ibrahim, Timo Weckman and Karoliina Honkala acknowledge the Jane and Aatos Erkko Foundation for funding the LACOR project. Electronic structure calculations were performed using computational resources provided by CSC—IT Center for Science, Espoo, Finland (https://www.csc.fi/en/), and computer capacity from the Finnish Grid and Cloud Infrastructure (urn:nbn:fi:research-infras-2016072533).

Appendix A. Supplementary data

Supplementary data to this article can be found online at https://doi.org/10.1016/j.cej.2024.158654.

Data availability

The experimental data presented is available on request from the corresponding author. The optimized computational structures are available for download through the IDA fair data service at the following link: https://etsin.fairdata.fi/dataset/77db9175-0c31-4892-8c99-752e3c626c09.

References

[1] WHO, UNICEF, Progress on household drinking water, sanitation and hygiene 2000-2020: five years into the SDGs, 2021.
[2] B.M.J.K. Balasooriya, J. Rajapakse, C. Gallage, A review of drinking water quality issues in remote and indigenous communities in rich nations with special emphasis on Australia, Sci. Total Environ. 903 (2023), https://doi.org/10.1016/j.scitotenv.2023.166559.
[3] X. Li, C. Wang, J. Zhang, J. Liu, B. Liu, G. Chen, Preparation and application of magnetic biochar in water treatment: A critical review, Sci. Total Environ. 711 (2020), https://doi.org/10.1016/j.scitotenv.2019.134847.
[4] X. Tan, Q. Peng, T. Subrova, J. Saskova, J. Wiener, M. Venkataraman, J. Militky, W. Xiong, J. Xu, A.R. Mahendran, H. Lammer, Characterization of Cellulose/Polyvinyl Alcohol/Expanded Graphite 3D Porous Foam and Adsorption of Methylene Blue, J. Nat. Fibers 20 (2023), https://doi.org/10.1080/15440478.2023.2190189.
[5] U. Chadha, S.K. Selvaraj, S. Vishak Thanu, V. Cholapadath, A.M. Abraham, M. Zaiyan M, M. Manoharan, V. Paramsivam, A review of the function of using carbon nanomaterials in membrane filtration for contaminant removal from wastewater, Mater Res Express 9 (2022). doi: 10.1088/2053-1591/ac48b8.
[6] H. Sultana, M. Usman, Surfactant-assisted flocculation for the efficient removal of aqueous dyestuff: A sustainable approach, J Mol Liq 370 (2023), https://doi.org/10.1016/j.molliq.2022.120988.
[7] Y. Li, Y. An, R. Zhao, Y. Zhong, S. Long, J. Yang, J. Li, H. Zheng, Synergetic removal of oppositely charged dyes by co-precipitation and amphoteric self-floating capturer: Mechanism investigation by molecular simulation, Chemosphere 296 (2022), https://doi.org/10.1016/j.chemosphere.2022.134033.
[8] R. Nandanwar, J. Bamne, N. Singh, K. Taiwade, V. Chandel, P.K. Sharma, P. Singh, A. Umar, F.Z. Haque, Synthesis of Titania-Silica Nanocomposite for Enhanced Photodegradation of Methylene Blue and Methyl Orange Dyes under UV and Mercury Lights, ES Materials and Manufacturing 16 (2022), https://doi.org/10.30919/esmm5f628.
[9] D. Pan, Y. Song, C. Liu, Z. Guo, Research Progress on Wastewater Treatment in Food Industry: A Mini-review, ES Food and Agroforestry 10 (2022), https://doi.org/10.30919/esfaf793.
[10] S. Soni, P.K. Bajpai, J. Mittal, C. Arora, Utilisation of cobalt doped Iron based MOF for enhanced removal and recovery of methylene blue dye from wastewater, J Mol Liq 314 (2020), https://doi.org/10.1016/j.molliq.2020.113642.
[11] T. Kuanyshbekov, N. Guseinov, B. Kurbanova, R. Nemkaeva, K. Akatan, Z. Tolepov, M. Tulegenova, M. Aitzhanov, E. Zhasasynov, S. Thomas, Local Natural Graphite as a Promising Raw Material for the Production of Thermally Reduced Graphene-Like Films, ES Materials and Manufacturing 23 (2024), https://doi.org/10.30919/esmm1000.
[12] R.D. Hunter, J. Ramírez-Rico, Z. Schnepp, Iron-catalyzed graphitization for the synthesis of nanostructured graphitic carbons, J Mater Chem A Mater 10 (2022), https://doi.org/10.1039/d1ta09654k.
[13] V.S. Sivasankarapillai, A. Sundararajan, M. Eswaran, R. Dhanusuraman, Hierarchical Porous Activated Carbon Derived from Callistemon viminalis Leaf Biochar for Supercapacitor and Methylene Blue Removal Applications, ES Energy and Environment 24 (2024), https://doi.org/10.30919/esee1124.

[14] L. Dai, Q. Lu, H. Zhou, F. Shen, Z. Liu, W. Zhu, H. Huang, Tuning oxygenated functional groups on biochar for water pollution control: A critical review, J Hazard Mater 420 (2021), https://doi.org/10.1016/j.jhazmat.2021.126547.

[15] J. Mosebolatan Jabar, Pyrolysis: A Convenient Route for Production of Eco-Friendly Fuels and Precursors for Chemical and Allied Industries, in: Recent Perspectives in Pyrolysis Research, 2022, https://doi.org/10.5772/intechopen.101068.

[16] B. Sajjadi, W.Y. Chen, N.O. Egiebor, A comprehensive review on physical activation of biochar for energy and environmental applications, Rev. Chem. Eng. 35 (2019), https://doi.org/10.1515/revce-2017-0113.

[17] L.S. Maia, L.D. Duizit, F.R. Pinhatio, D.R. Mulinari, Valuation of banana peel waste for producing activated carbon via NaOH and pyrolysis for methylene blue removal, Carbon Letters 31 (2021), https://doi.org/10.1007/s42823-021-00226-5.

[18] S.M. Kakom, N.M. Abdelmonem, I.M. Ismail, A.A. Refaat, Activated Carbon from Sugarcane Bagasse Pyrolysis for Heavy Metals Adsorption, Sugar Tech 25 (2023), https://doi.org/10.1007/s12355-022-01214-3.

[19] Y. Qiu, X. Xu, Z. Xu, J. Liang, Y. Yu, X. Cao, Contribution of different iron species in the iron-biochar composites to sorption and degradation of two dyes with varying properties, Chem. Eng. J. 389 (2020), https://doi.org/10.1016/j.cej.2020.124471.

[20] N. Zhao, F. Chang, B. Hao, L. Yu, J.L. Morel, J. Zhang, Removal of organic dye by biomass-based iron carbide composite with an improved stability and efficiency, J Hazard Mater 369 (2019), https://doi.org/10.1016/j.jhazmat.2019.02.077.

[21] Z. Cai, J. Liu, B. Chen, Y. Song, X. Xu, S. You, F. Song, X. Wang, J. Zou, Need a balance? relationship between removal reactivity of cationic dye and bacterial cytotoxicity by iron carbide-stabilized nano zero-valent iron, Chem. Eng. J. 452 (2023), https://doi.org/10.1016/j.cej.2022.139150.

[22] T.A. Wezendonk, V.P. Santos, M.A. Nasalevich, Q.S.E. Warringa, A.I. Dugulan, A. Chojecki, A.C.J. Koeken, M. Ruitenbeek, G. Meima, H.U. Islam, G. Sankar, M. Makkee, F. Kapteijn, J. Gascon, Elucidating the Nature of Fe Species during Pyrolysis of the Fe-BTC MOF into Highly Active and Stable Fischer-Tropsch Catalysts, ACS Catal 6 (2016), https://doi.org/10.1021/acscatal.6b00426.

[23] J.Q. Sun, S.K. Zheng, J.G. Chen, Influence of pretreatment conditions on the structure and catalytic performance of supported cobalt catalysts derived from metal-organic frameworks, Ranliao Huaxue Xuebao/journal of Fuel Chemistry and Technology 51 (2023) 1291–1297, https://doi.org/10.1016/S1872-5813(23)60352-4.

[24] I.S. Khan, L. Garzon-Tovar, D. Mateo, J. Gascon, Metal-Organic-Frameworks and Their Derived Materials in Photo-Thermal Catalysis, Eur J Inorg Chem 2022 (2022), https://doi.org/10.1002/ejic.202200316.

[25] A. Ahmad, S. Shaheen, S. Majeed, M. Pervaiz, Z. Saeed, U. Younas, M.S. Javed, R. Luque, L. Gnanasekaran, Recent developments in metal/metalloid nanomaterials for battery applications; a comparative review, Fuel 340 (2023), https://doi.org/10.1016/j.fuel.2023.127399.

[26] V. Gascón, M.B. Jiménez, R.M. Blanco, M. Sanchez-Sanchez, Semi-crystalline Fe-BTC MOF material as an efficient support for enzyme immobilization, Catal Today 304 (2018), https://doi.org/10.1016/j.cattod.2017.10.022.

[27] S. Hegazy, M. Manninen, S. Tuomikoski, U. Lassi, V. Srivastava, Nano-impregnation on metakaolin backbone for enhanced removal of Cu(II) and Mn(II) ions in a binary system using fixed bed column, Sep Purif Technol 329 (2024), https://doi.org/10.1016/j.seppur.2023.125163.

[28] S.A. Messele, O.S.G.P. Soares, J.J.M. Órfão, F. Stüber, C. Bengoa, A. Fortuny, A. Fabregat, J. Font, Zero-valent iron supported on nitrogen-containing activated carbon for catalytic wet peroxide oxidation of phenol, Appl Catal B 154–155 (2014), https://doi.org/10.1016/j.apcatb.2014.02.033.

[29] P. Shah, S. Kumari Jha, A. Bhattarai, Spectrophotometric study of the sodium dodecyl sulfate in the presence of methylene blue in the methanol–water mixed solvent system, J Mol Liq 340 (2021), https://doi.org/10.1016/j.molliq.2021.117200.

[30] M. Manninen, T. Kangas, T. Hu, T. Varila, U. Lassi, H. Runtti, Zn(II) removal from wastewater by an alkali-activated material prepared from steel industry slags: optimization and modelling of a fixed-bed process, Environmental Technology (united Kingdom) (2023), https://doi.org/10.1080/09593330.2023.2177565.

[31] F. Zietzschmann, Neuauflage: Adsorption Technology in Water Treatment, Vom Wasser 119 (2021), https://doi.org/10.1002/vomw.202170307.

[32] J. Enkovaara, C. Rostgaard, J.J. Mortensen, J. Chen, M. Du\textbackslashlak, L. Ferrighi, J. Gavnholt, C. Glinsvad, V. Haikola, H.A. Hansen, H.H. Kristoffersen, M. Kuisma, A.H. Larsen, L. Lehtovaara, M. Ljungberg, O. Lopez-Acevedo, P. G. Moses, J. Ojanen, T. Olsen, V. Petzold, N.A. Romero, J. Stausholm-Møller, M. Strange, G.A. Tritsaris, M. Vanin, M. Walter, B. Hammer, H. Häkkinen, G.K. H. Madsen, R.M. Nieminen, J.K. Nørskov, M. Puska, T.T. Rantala, J. Schiøtz, K. S. Thygesen, K.W. Jacobsen, Electronic structure calculations with GPAW: a real-space implementation of the projector augmented-wave method, J. Phys.: Condens. Mat. 22 (2010) 253202, https://doi.org/10.1088/0953-8984/22/25/253202.

[33] J.J. Mortensen, A.H. Larsen, M. Kuisma, A.V. Ivanov, A. Taghizadeh, A. Peterson, A. Haldar, A.O. Dohn, C. Schäfer, E.Ö. Jónsson, E.D. Hermes, F.A. Nilsson, G. Kastlunger, G. Levi, H. Jónsson, H. Häkkinen, J. Fojt, J. Kangsabanik, J. Sødequist, J. Lehtomäki, J. Heske, J. Enkovaara, K.T. Winther, M. Dulak, M. M. Melander, M. Ovesen, M. Louhivuori, M. Walter, M. Gjerding, O. Lopez-Acevedo, P. Erhart, R. Warmbier, R. Würdemann, S. Kaappa, S. Latini, T.M. Boland, T. Bligaard, T. Skovhus, T. Susi, T. Maxson, T. Rossi, X. Chen, Y.L.A. Schmerwitz, J. Schiøtz, T. Olsen, K.W. Jacobsen, K.S. Thygesen, GPAW: An open Python package for electronic structure calculations, J Chem Phys 160 (2024) 92503, https://doi.org/10.1063/5.0182685.

[34] J.P. Perdew, K. Burke, M. Ernzerhof, Generalized Gradient Approximation Made Simple, PhysRevLett 77 (1996) 3865–3868, https://doi.org/10.1103/PhysRevLett.77.3865.

[35] E. Caldeweyher, J.-M. Mewes, S. Ehlert, S. Grimme, Extension and evaluation of the D4 London-dispersion model for periodic systems, PCCP 22 (2020) 8499–8512, https://doi.org/10.1039/D0CP00502A.

[36] V. Korpelin, M.M. Melander, K. Honkala, Reducing the Irreducible: Dispersed Metal Atoms Facilitate Reduction of Irreducible Oxides, J. Phys. Chem. C 126 (2022) 933–945, https://doi.org/10.1021/acs.jpcc.1c08979.

[37] A.I. Liechtenstein, V.I. Anisimov, J. Zaanen, Density-functional theory and strong interactions: Orbital ordering in Mott-Hubbard insulators, PhysRevB 52 (1995) R5467–R5470, https://doi.org/10.1103/PhysRevB.52.R5467.

[38] S.L. Dudarev, G.A. Botton, S.Y. Savrasov, C.J. Humphreys, A.P. Sutton, Electron-energy-loss spectra and the structural stability of nickel oxide: An LSDA+U study, PhysRevB 57 (1998) 1505–1509, https://doi.org/10.1103/PhysRevB.57.1505.

[39] A. Held, M. Walter, Simplified continuum solvent model with a smooth cavity based on volumetric data, J Chem Phys 141 (2014) 174108, https://doi.org/10.1063/1.4900838.

[40] G. Kastlunger, P. Lindgren, A.A. Peterson, Controlled-Potential Simulation of Elementary Electrochemical Reactions: Proton Discharge on Metal Surfaces, J. Phys. Chem. C 122 (2018) 12771–12781, https://doi.org/10.1021/acs.jpcc.8b02465.

[41] C. Kittel, Introduction to solid state physics, 8. ed., [repr.],, Wiley, Hoboken, NJ, 2005.

[42] W.P. Davey, Precision measurements of the lattice constants of twelve common metals, Phys. Rev. 25 (1925) 753–761, https://doi.org/10.1103/PhysRev.25.753.

[43] A. Tsuzuki, S. Sago, S.-I. Hirano, S. Naka, High temperature and pressure preparation and properties of iron carbides Fe_7C_3 and Fe_3C, J Mater Sci 19 (1984) 2513–2518, https://doi.org/10.1007/BF00550805.

[44] I.N. Shabanova, V.A. Trapeznikov, Temperature dependence of the intensity of the characteristic energy losses of 2p electrons of iron in cementite, ZhETF Pisma Redaktsiiu 18 (1973) 576.

[45] W.C. Chiou, E.A. Carter, Structure and stability of Fe_3C-cementite surfaces from first principles, Surf Sci 530 (2003) 88–100, https://doi.org/10.1016/S0039-6028(03)00352-2.

[46] L.W. Finger, R.M. Hazen, A.M. Hofmeister, High-Pressure crystal chemistry of spinel ($MgAl_2O_4$) and magnetite (Fe_3O_4): Comparisons} with silicate spinels, Phys Chem Miner 13 (1986) 215–220, https://doi.org/10.1007/BF00308271.

[47] H. Okudera, K. Kihara, T. Matsumoto, Temperature dependence of structure parameters in natural magnetite: single crystal X-ray studies from 126 to 773 K, Acta Crystallogr B 52 (1996) 450–457, https://doi.org/10.1107/S0108768196000845.

[48] X. Yu, C.-F. Huo, Y.-W. Li, J. Wang, H. Jiao, Fe_3O_4 surface electronic structures and stability from GGA+U, Surf Sci 606 (2012) 872–879, https://doi.org/10.1016/j.susc.2012.02.003.

[49] V.N. Petrov, A.B. Ustinov, Magnetic properties of Fe_3O_4 surface, Journal of Surface Investigation 4 (2010) 395–400, https://doi.org/10.1134/S1027451010030079.

[50] K. Jordan, A. Cazacu, G. Manai, S.F. Ceballos, S. Murphy, I.V. Shvets, Scanning tunneling spectroscopy study of the electronic structure of Fe_3O_4 surfaces, PhysRevB 74 (2006) 85416, https://doi.org/10.1103/PhysRevB.74.085416.

[51] A.R. Lennie, N.G. Condon, F.M. Leibsle, P.W. Murray, G. Thornton, D.J. Vaughan, Structures of Fe_3O_4 (111) surfaces observed by scanning tunneling microscopy, PhysRevB 53 (1996) 10244–10253, https://doi.org/10.1103/PhysRevB.53.10244.

[52] X. Li, J. Paier, Adsorption of Water on the Fe_3O_4(111) Surface: Structures, Stabilities, and Vibrational Properties Studied by Density Functional Theory, J. Phys. Chem. C 120 (2016) 1056–1065, https://doi.org/10.1021/acs.jpcc.5b10560.

[53] S. Munir, M. Amin, N. Iqbal, A. Iqbal, A.A. Ghfar, Effect of Pyrolysis on iron-metal organic frameworks (MOFs) to Fe_3C @ Fe_5C_2 for diesel production in Fischer-Tropsch Synthesis, Front Chem 11 (2023), https://doi.org/10.3389/fchem.2023.1150565.

[54] M. Thommes, K. Kaneko, A.V. Neimark, J.P. Olivier, F. Rodriguez-Reinoso, J. Rouquerol, K.S.W. Sing, Physisorption of gases, with special reference to the evaluation of surface area and pore size distribution (IUPAC Technical Report), Pure Appl. Chem. 87 (2015), https://doi.org/10.1515/pac-2014-1117.

[55] X. Yang, B. Fei, J. Ma, X. Liu, S. Yang, G. Tian, Z. Jiang, Porous nanoplatelets wrapped carbon aerogels by pyrolysis of regenerated bamboo cellulose aerogels as supercapacitor electrodes, Carbohydr Polym 180 (2018), https://doi.org/10.1016/j.carbpol.2017.10.013.

[56] N.Y. Yao, J.P. Cao, J.P. Zhao, Z.M. He, X.B. Feng, T.L. Liu, Z.Y. Wang, X.Y. Zhao, Efficient and selective catalytic pyrolysis of cellulose to monocyclic aromatic hydrocarbons over Zn-containing HZSM-5, Fuel 310 (2022), https://doi.org/10.1016/j.fuel.2021.122437.

[57] Y. Tang, K. Petropoulos, F. Kurth, H. Gao, D. Migliorelli, O. Guenat, S. Generelli, Screen-Printed Glucose Sensors Modified with Cellulose Nanocrystals (CNCs) for Cell Culture Monitoring, Biosensors (basel) 10 (2020), https://doi.org/10.3390/bios10090125.

[58] J.H. Ong, Y.N. Liang, X. Hu, R. Xu, TEMPO-Oxidized Microcrystalline Cellulose for Rapid Adsorption of Ammonium, Ind Eng Chem Res 61 (2022), https://doi.org/10.1021/acs.iecr.1c04599.

[59] L. Das, P. Das, A. Bhowal, C. Bhattacharjee, Enhanced biosorption of fluoride by extracted nanocellulose/polyvinyl alcohol composite in batch and fixed-bed system: ANN analysis and numerical modeling, Environ. Sci. Pollut. Res. 28 (2021), https://doi.org/10.1007/s11356-021-14026-x.

[60] G.R. Delpiano, D. Tocco, L. Medda, E. Magner, A. Salis, Adsorption of malachite green and alizarin red s dyes using Fe-BTC metal organic framework as adsorbent, Int J Mol Sci 22 (2021), https://doi.org/10.3390/ijms22020788.

[61] H. Lu, L. Zhang, B. Wang, Y. Long, M. Zhang, J. Ma, A. Khan, S.P. Chowdhury, X. Zhou, Y. Ni, Cellulose-supported magnetic Fe_3O_4–MOF composites for enhanced

dye removal application, Cellul. 26 (2019), https://doi.org/10.1007/s10570-019-02415-y.
[62] M. Wang, C. Shao, S. Zhou, J. Yang, F. Xu, Preparation of carbon aerogels from TEMPO-oxidized cellulose nanofibers for organic solvents absorption, RSC Adv 7 (2017) 38220–38230, https://doi.org/10.1039/c7ra05506d.
[63] B. Pangkumhang, P. Jutaporn, K. Sorachoti, P. Khamdahsag, V. Tanboonchuy, Applicability of iron (III) Trimesic (Fe-BTC) to enhance lignin separation from pulp and paper wastewater, Sains Malays 48 (2019), https://doi.org/10.17576/jsm-2019-4801-23.
[64] S. Chen, Z. Zang, S. Zhang, G. Ouyang, R. Han, Preparation of MIL-100(Fe) and multi-walled carbon nanotubes nanocomposite with high adsorption capacity towards Oxytetracycline from solution, J Environ Chem Eng 9 (2021), https://doi.org/10.1016/j.jece.2020.104780.
[65] A. Velázquez-Palenzuela, L. Zhang, L. Wang, P.L. Cabot, E. Brillas, K. Tsay, J. Zhang, Carbon-Supported Fe-Nx catalysts synthesized by pyrolysis of the Fe(II)-2,3,5,6-tetra(2-pyridyl)pyrazine complex: Structure, electrochemical properties, and oxygen reduction reaction activity, J. Phys. Chem. C 115 (2011), https://doi.org/10.1021/jp2020897.
[66] M. Hosseini Talari, N.S. Tabrizi, V. Babaeipour, F. Halek, Adsorptive removal of organic pollutants from water by carbon fiber aerogel derived from bacterial cellulose, J Solgel Sci Technol 101 (2022), https://doi.org/10.1007/s10971-021-05708-6.
[67] L. Liu, Z.Y. Gao, X.P. Su, X. Chen, L. Jiang, J.M. Yao, Adsorption removal of dyes from single and binary solutions using a cellulose-based bioadsorbent, ACS Sustain Chem Eng 3 (2015), https://doi.org/10.1021/sc500848m.
[68] X. He, K.B. Male, P.N. Nesterenko, D. Brabazon, B. Paull, J.H.T. Luong, Adsorption and desorption of methylene blue on porous carbon monoliths and nanocrystalline cellulose, ACS Appl Mater Interfaces 5 (2013), https://doi.org/10.1021/am403222u.
[69] T. Shimizu, K.K.H. De Silva, M. Hara, M. Yoshimura, Facile synthesis of carbon nanotubes and cellulose nanofiber incorporated graphene aerogels for selective organic dye adsorption, Appl Surf Sci 600 (2022), https://doi.org/10.1016/j.apsusc.2022.154098.
[70] M. Ghaedi, S.N. Kokhdan, Removal of methylene blue from aqueous solution by wood millet carbon optimization using response surface methodology, Spectrochim Acta A Mol Biomol Spectrosc 136 (2015), https://doi.org/10.1016/j.saa.2014.07.048.
[71] L. Leng, X. Yuan, G. Zeng, J. Shao, X. Chen, Z. Wu, H. Wang, X. Peng, Surface characterization of rice husk biochar produced by liquefaction and application for cationic dye (Malachite green) adsorption, Fuel 155 (2015), https://doi.org/10.1016/j.fuel.2015.04.019.
[72] Z. Li, Z. Jia, T. Ni, S. Li, Adsorption of methylene blue on natural cotton based flexible carbon fiber aerogels activated by novel air-limited carbonization method, J Mol Liq 242 (2017), https://doi.org/10.1016/j.molliq.2017.07.062.
[73] Y. Zheng, P. Lv, J. Yang, G. Xu, Characterization and Adsorption Capacity of Modified Biochar for Sulfamethylimidine and Methylene Blue in Water, ACS Omega (2023), https://doi.org/10.1021/acsomega.3c01251.
[74] H.V. Le, N.T. Dao, H.T. Bui, P.T. Kim Le, K.A. Le, A.T. Tuong Tran, K.D. Nguyen, H. H. Mai Nguyen, P.H. Ho, Bacterial Cellulose Aerogels Derived from Pineapple Peel Waste for the Adsorption of Dyes, ACS Omega 8 (2023), https://doi.org/10.1021/acsomega.3c03130.
[75] P. Joshi, A. Prolta, S. Mehta, T.S. Khan, M. Srivastava, O.P. Khatri, Adsorptive removal of multiple organic dyes from wastewater using regenerative microporous carbon: Decisive role of surface-active sites, charge and size of dye molecules, Chemosphere 308 (2022), https://doi.org/10.1016/j.chemosphere.2022.136433.